

Broadband Coding Metasurfaces with 2-bit Manipulations

Sheng-Dong Zhao,^{1,2} Hao-Wen Dong,^{3,*} Xuan-Bo Miao,⁴ Yue-Sheng Wang,^{4,5,†} and Chuanzeng Zhang^{6,‡}

¹*School of Mathematics and Statistics, Qingdao University, Qingdao 266071, People's Republic of China*


²*Institute of Mechanics for Multifunctional Materials and Structures, Qingdao University, Qingdao 266071, People's Republic of China*

³*Institute of Advanced Structure Technology, Beijing Institute of Technology, Beijing 100081, People's Republic of China*

⁴*Department of Mechanics, School of Mechanical Engineering, Tianjin University, Tianjin 300350, People's Republic of China*

⁵*Institute of Engineering Mechanics, Beijing Jiaotong University, Beijing 100044, China*

⁶*Department of Civil Engineering, University of Siegen, D-57068 Siegen, Germany*

 (Received 1 October 2021; revised 20 November 2021; accepted 11 February 2022; published 7 March 2022)

Due to their limited number of units but outstanding ability to control rather complex wave-propagation phenomena, acoustic coding metasurfaces (ACMs) as two-dimensional metamaterials show a stronger competitiveness in metamaterial applications. However, hindered by their narrow-band modulation capability, the previously reported ACMs do not exhibit a broadband applicability. To address the frequency-based coding capability, in this paper we report broadband acoustic coding metasurfaces (BACMs) whose units are designed by the bottom-up topology optimization method. Subsequently, by utilizing our optimization strategy, we design the 1-bit coding units “0” and “1” with out-of-phase responses and the 2-bit coding units “00”, “01”, “10,” and “11” with four different phase shifts of 0°, 90°, 180°, and 270°. The topological features show constant phase differences, and in the following analysis, we attempt to explain this phenomenon by the related mechanisms of the internal resonances and the bianisotropy effect. The optimized BACMs are beneficial to improve the functions of a fixed coding metasurface in the frequency range. This idea provides an inspiration for fabricating fast-sector-scanning sound antenna. In combination with the convolution method, we also present the design strategy for the broadband fast-scanning multiple-beam antenna. The design of the acoustic antenna is a fixed coding sequence, and its scanning and echolocation mode does not depend on the reconfiguration of the coding units. Furthermore, we also demonstrate a pair of opposite functions, namely the broadband sound focusing and diffusion-scattering characteristics, which have potential applications in ultrasonic therapy, low-scattering target design and noise control, and so on.

DOI: [10.1103/PhysRevApplied.17.034019](https://doi.org/10.1103/PhysRevApplied.17.034019)

I. INTRODUCTION

Recent years have witnessed a rapid development in the field of metasurfaces, which are acquired by compressing the thickness and structural complexity of bulk metamaterials to two-dimensional (2D) scale [1–9]. Several striking features, such as the subwavelength scale [2], tangential phase controllability [7,8], and even transmittance modulation [10], provide us more space for wave manipulation (optical waves [1], acoustic waves [4], and even elastic waves [11]). The concept of metasurfaces was proposed in the optical field and the generalized Snell law

provides us with theoretical guidance. Alternative surprising applications were opened up by metasurfaces and, for many years, the increased research on metasurfaces was in the ascendant. As 2D subwavelength metamaterials, metasurfaces mainly provide nontrivial local phase shifts, which highlights their ability to freely tailor the wave fields. Such great features have revealed numerous intriguing properties, such as anomalous reflection and refraction [12,13], noise control [14,15], carpet cloaking [16,17], perfect sound absorbing [18], Schroeder diffusion [19], asymmetric transmission [10], vortex beam [20,21], and focusing [7–9]. At the same time, the introduction of deep learning [22,23] also brings opportunities for metasurface design.

Based on the effective medium theory, the aforementioned metamaterials or metasurfaces with

*hwdong@bit.edu.cn

†yswang@tju.edu.cn

‡c.zhang@uni-siegen.de

continuously varying macroscopic properties can be classified as “analog metamaterials.” Recently, the concept of “metamaterial bytes” implemented through proper spatial mixtures of “digital metamaterial bits” was presented by Della Giovampaola and Engheta [24]. Subsequently, Cui *et al.* [25] further clarified the general concepts of “coding metamaterial,” “digital metamaterial,” and “programmable metamaterial.” The digital metamaterial is assembled by the distinct coding units named “0” and “1” that have opposite phases; and the 2-bit coding metasurface is constructed by four coding units “00”, “01”, “10”, and “11”, exhibiting 0° , 90° , 180° , and 270° phase responses, respectively. With less variety of metasurface elements, coding metasurface design could be greatly simplified, and the various functionalities, such as directional antenna [25–29], focusing [27,30,31], and diffusion scattering [32–35] can be simply implemented by the corresponding coding sequences.

However, broadband features still remain challenging in metasurface design and from the practical viewpoint, a broadband metasurface with customized dispersion is required. In recent works, the integrated resonant unit is introduced to design broadband optical achromatic devices [36–39] whose performance still relies on the achromatic phase modulation of the units. The inverse-design methodology has shown a strong competitiveness in the field of broadband design [40–42]. Our latest work [43] expanded the ultrabroadband capability to acoustic metasurfaces; and a customized dispersion for the units was achieved by the optimization method, which ultimately leads to the desired broadband frequency-independent functionalities featuring a record-breaking relative bandwidth about 100%. In order to further expand the connotation of broadband metasurfaces, in this paper, we propose an optimization-based technology to design 1-bit and 2-bit broadband acoustic coding metasurfaces (BACMs) and demonstrate several performances numerically and experimentally, including broadband sound antenna, broadband focusing, and diffusion scattering. The customized dispersion units of the BACMs with constant phase differences have a higher degree of design difficulty, especially in exploring the transmission-type BACMs. This apparently calls for a coding-unit design method and leaves us a huge potential space to explore the BACMs relying on the customized inverse-design approaches. To date, these optimized coding units present one of the first examples of the BACMs for coded acoustic antenna and field manipulation. The optimized design in this paper advances the application of metasurface in acoustic control field such as broadband acoustic antenna. In our future research, we will also consider other challenging engineering applications such as ultrasonic [44] and underwater acoustic fields [45–47], which will lead to more innovative technological advances.

II. DESIGN OF THE METASURFACE UNITS BY TOPOLOGY OPTIMIZATION

Topology optimization has been widely used in the field of metamaterial design, and many metastructures including metasurfaces with alternative functions have been realized. Indeed, different optimization problems in the metamaterial design have different objectives and physical mechanisms. The realization of any successful optimization is possible only if a mathematical model encompassing specific objective functions and constraints is properly set. Many previous metamaterial optimization designs mainly focus on the broadband gaps, double negative metastructures and specific modulus design, and so on. It is not our intention to develop a completely alternative topology optimization method in this work. Instead, we define particular objective functions and constraints as described in what follows, which are aiming at constant phase differences and totally different from previous works. Concisely speaking, the focus of this paper is not the topology optimization method itself, but the inverse design of the broadband coding units, which can realize the constant phase differences in a wide frequency range with a relatively high transmission.

To construct the transmission-type BACMs with the constant phase differences (0° and 180° phase-response units for 1-bit BACM; 0° , 90° , 180° , and 270° phase-response units for 2-bit BACM), and at the same time guarantee a certain transmittance, we employ topology optimization to systematically design the demanding metasurface units. In addition, some geometrical constraints are also adopted in our optimization program to restrict the minimum size, e.g., the minimal solid components should guarantee the sufficient strength and manufacturing feasibility, and there should be no conspicuous viscous dissipation in the narrowest air channel.

A. Optimization parameter setting

To systemically design the required coding metasurface units, it is effective and robust to perform topology optimization for the unit with the prescribed phase-shift property. To realize the broadband coding manipulation, two arbitrary metasurface units should maintain a constant phase difference, such as 90° , 180° , and 270° . At this point, the target frequency range $[f_{\min}, f_{\max}]$ can be divided into a certain number of sampling frequencies. Therefore, the optimization objective is converted into minimizing the difference between the target phase shift and the actual one at all discrete frequencies. It is generally difficult to maintain a fixed phase difference over a certain frequency range with metamaterial elements. However, our optimal design of the units can overcome the unpredictability dispersion and then achieve customized dispersion characteristics that meet the rigorous requirements. To ensure the relatively high transmission, the averaged transmission coefficient

should be larger than 0.6 within the target frequency range. It is difficult to achieve high transmittance in the broadband frequency range with the antiphase unit of 180° , so we use an average transmittance larger than 0.6 over the broadband, and there are some frequencies where the transmittance is slightly lower than 0.6. The transmission difference of the units will lead to distortion of the preset sound field to a certain extent, however, the following numerical simulation and experimental results confirm that the above transmittance conditions have not significantly changed the phenomenon of the sound regulation.

We use the genetic algorithm (GA) [43] to solve this optimization problem. A metasurface unit can be treated as an individual, which is composed of 240×60 design variables. First, a population consisting of N_p binary individuals is randomly generated. Then, the “abuttal entropy filter” is applied to all individuals to eliminate the traditional checkerboard pattern and improve the topologies. Secondly, the fitness and constraint satisfaction of every individual is evaluated according to the phase-matching extent and the averaged transmission. Thirdly, a series of genetic operations including selection, crossover, and mutation are employed to all individuals in the current

generation to produce the offspring population. Fourthly, the elitism strategy is introduced in optimization to accelerate the evolution. Finally, the whole evolution will stop and give rise to an optimized unit when the generation number is equal to the presupposed one.

B. Objective functions and constraints

To construct the transmission-type BACMs with constant phase differences (0° and 180° units for 1-bit BACM; 0° , 90° , 180° , and 270° phase-response units for 2-bit BACM), and at the same time guarantee a certain transmittance, we employ topology optimization to systematically design the demanding metasurface units. In addition, geometric constraints are also adopted in our optimization program to restrict the minimum size, such as the minimal solid component should guarantee the sufficient strength and manufacturing compatibility and there should be no conspicuous viscous dissipation in the narrowest air channel. To address the above requirements, the single-objective optimization with multiple constraints for a 2D rectangular design domain (Fig. 1) is formulated as follows [43]:

$$\text{for } f_i \in [f_{\min}, f_{\max}] \quad (i = 1, 2 \cdots N_F), \quad (1)$$

$$\begin{aligned} \text{minimize } O(\Omega_D) = & \frac{1}{2\pi} \max \\ & \times \left\{ \sqrt{\frac{(\phi_D^1 + \phi_D^2 + \cdots + \phi_D^{N_F})}{N_F}} \times \max(\phi_D^1, \phi_D^2 \cdots \phi_D^{N_F}), \sqrt{\left[\frac{1}{N_F} \sum_{i=1}^{N_F} \left(\phi_D^i - \frac{\sum_{i=1}^{N_F} (\phi_D^i)}{N_F} \right)^2 \right]} \times \max(\phi_D^1, \phi_D^2 \cdots \phi_D^{N_F}) \right\}, \end{aligned} \quad (2)$$

$$\begin{aligned} \text{subject to } \rho_i = 0 \text{ or } 1 \quad (i = 1, 2 \cdots N_E), \\ \Omega_A \geq 1, \\ \min_{\Omega_D}(\mathbf{R}_A) \geq t_A, \\ \min_{\Omega_D}(\mathbf{R}_S) \geq t_S, \\ T(\Omega_D) \geq 0.6, \end{aligned} \quad (3)$$

where the sampling frequency number in the target frequency range $[f_{\min}, f_{\max}]$ is $(N_F - 1)$, which are uniformly distributed over the whole range; Ω_D is the 2D design domain; ϕ_D^i characterizes the absolute difference between the desired and theoretical phases at the i th sampling frequency; ρ_i represents the material density 0 (1) of a finite

element of air (solid); N_E are numbers of the finite elements; Ω_A is the number of the connected air domains and the air channel is connected from the left side of the unit to the right port to ensure that sound waves can pass through; \mathbf{R}_A and \mathbf{R}_S represent arrays consisting of local air and solid blocks, respectively; t_A and t_S are the prescribed test values

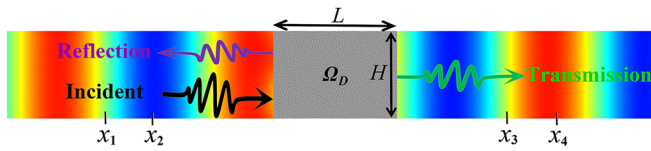


FIG. 1. The computational model used in the coding units' optimization progress. The gray area Ω_D is the optimization design domain. In simulation, the periodic boundary conditions are imposed on the top and bottom boundaries of the model. Nonreflecting boundaries are introduced on the left and right ports.

[40,41]; T is an averaged transmission coefficients within the targeted range.

Figure 1 is the topology optimization model utilized in our paper, where Ω_D is the design domain with the size of $W \times H$ that is meshed by $N_{EX} \times N_{EY}$ 4-node linear quadrilateral finite elements (AC2D4) in ABAQUS 6.14-1. To avoid acoustic coupling between the optimized units, we add a layer of solid wall on the top and bottom boundaries of the design domain. The plane waves are incident in the

model from the left port and the transmission coefficient is calculated based on the classical four-microphone method [48]. The microphones are placed at the positions of x_1 , x_2 , x_3 , and x_4 , as shown in Fig. 1. The geometric sizes of H and W in optimization take the values of 4 and 6 cm, respectively.

The material parameters used in optimization are $\rho_{\text{air}} = 1.29 \text{ kg/m}^3$, $c_{\text{air}} = 343 \text{ m/s}$, $\rho_{\text{solid}} = 1230 \text{ kg/m}^3$, and $c_{\text{solid}} = 2230 \text{ m/s}$. Because of the high impedance mismatch between the solid and air, generally, the solid can be assumed to be acoustically hard to simplify the optimization. Thus, the four 2-bit optimization units are customized as shown in Fig. 2(a). The broadband phase differences and the transmission spectra of the four units are present in Figs. 2(b) and 2(c) and the relative bandwidth namely the ratio of the bandwidth to its central frequency reaches 46%.

To clarify the physical mechanism of the broadband phase modulations, we prudently study the topological features and it can be found that the optimized asymmetrical units are composed of multicavity and complex coiling channels.

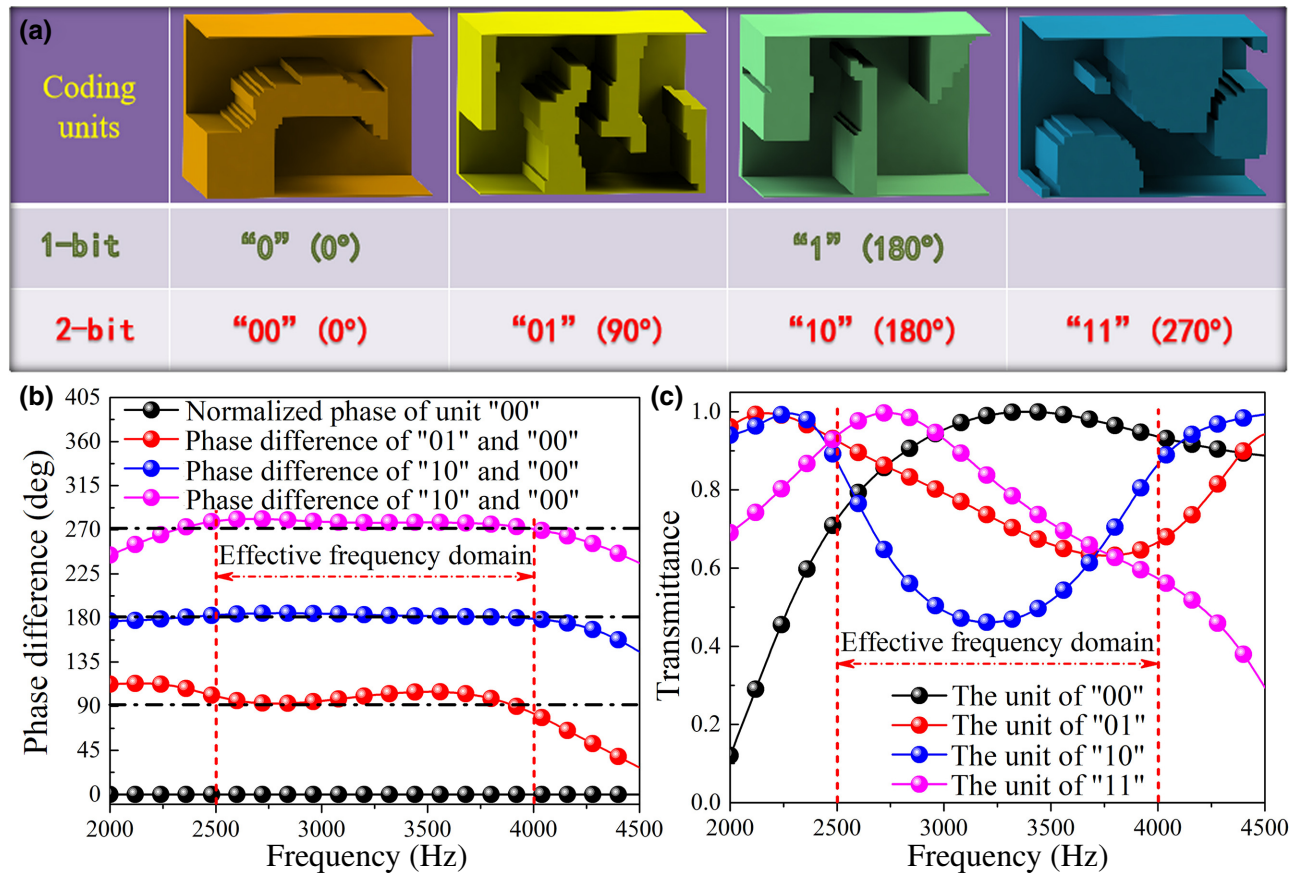


FIG. 2. The 1-bit and 2-bit optimized coding units and the corresponding broadband phase differences and transmission spectra. (a) The 3D-printed four units achieved by stretching the optimized 2D topology along the axial direction. (b) The broadband phase differences of the four units in (a), where the phase of the unit "00" is normalized to 0. (c) The transmission spectra of the four units.

The topological features revealed in this paper are different from the traditional Helmholtz-resonator and space-coiling-type acoustic metasurfaces; and the constant phase difference is generated by the combination of the internal resonances and the bianisotropy effect.

The geometry of the four asymmetrical units shares the similar characteristics, e.g., the irregular resonant cavities and complex connecting channels. The simulation results show that there are multiple internal resonance modes within the frequency range of interest [see insets of Fig. 3(a)]. Therefore, as the transmission characteristic is affected by the unit resonance, the internal resonance should play a role in the respective frequency bands, which leads to the broadband effect. In addition, the underlying mechanism of the broadband effect is rather complex,

and there may be other mechanisms that contribute to the overall property of the metasurface, including the bianisotropy.

At the beginning of our design, the structural asymmetry is intentionally embedded to keep a high degree of freedom to design more complex structures. In other words, the designed unit cells are asymmetric in their geometry, which could lead to a bianisotropy in general. Our design results show that the optimized units exhibit in fact an asymmetry and a bianisotropy. Here, bianisotropy refers to the phenomenon that when sound waves are incident from opposite directions, the corresponding sound responses at both ends of the structure are different, which is therefore generally utilized to achieve directional wave control. Furthermore, the impedance matrix

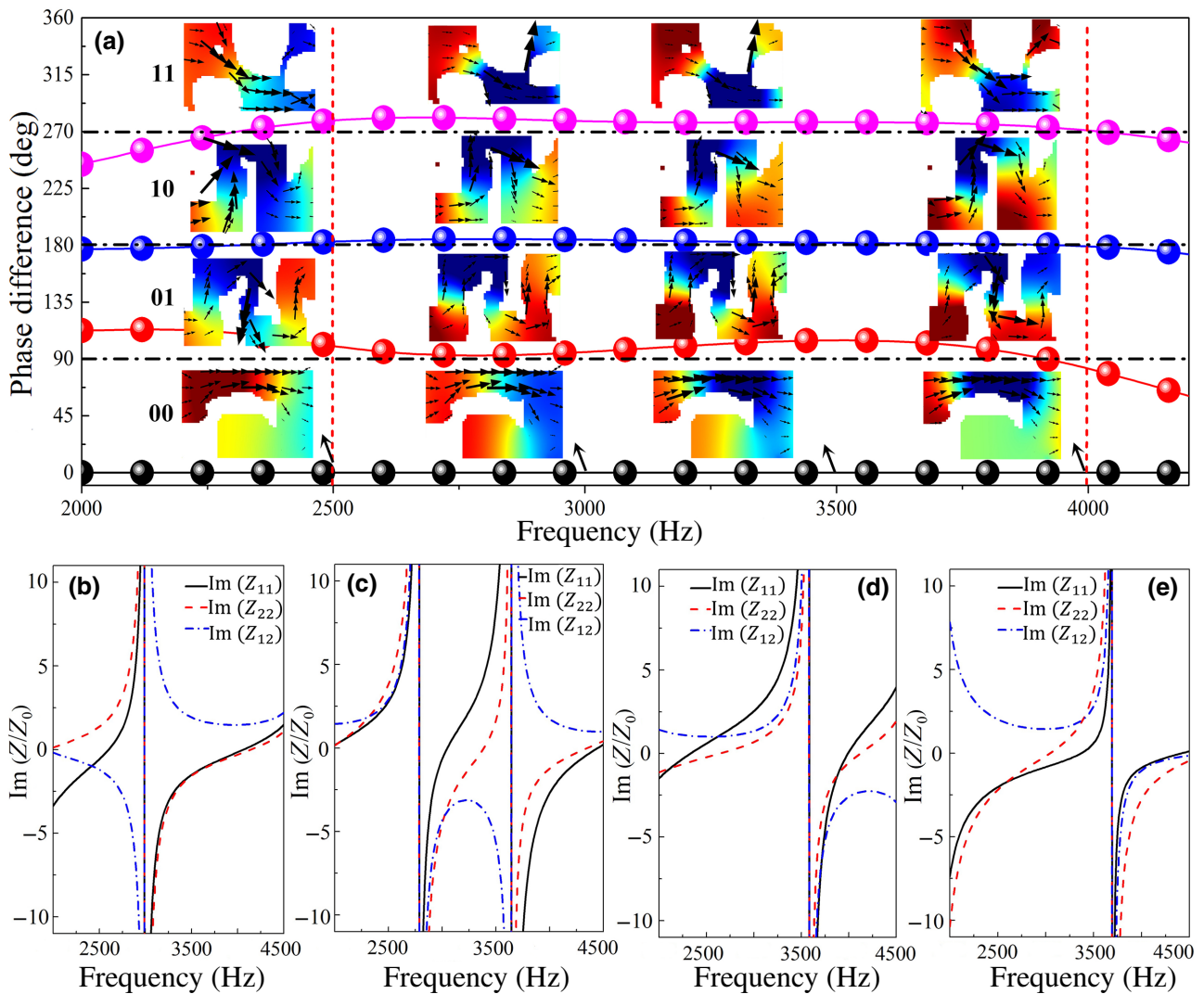


FIG. 3. Broadband wave characterizations of the four coding units. (a) Theoretical and optimized phase differences of the four coding units [Fig. 2(b)]. The insets display the acoustic pressure fields and the energy flux directions of the optimized units. These internal resonances contribute to the rigorous phase compensations at different frequencies. (b)–(e) Impedance spectra of the four optimized coding units of “00” (b), “01” (c), “10” (d), and “11” (e), where Z_0 is the impedance of air.

of $\mathbf{Z} = \begin{bmatrix} Z_{11} & Z_{12} \\ Z_{21} & Z_{22} \end{bmatrix}$ can be used to explain the bianisotropy effects caused by the asymmetry of the optimized units. Here, Z_{ij} are the components of impedance matrix and if $Z_{11} \neq Z_{22}$, the unit will show bianisotropic response [49]. The results in Figs. 3(b)–3(e) reveal that the four coding units exhibit a bianisotropy property with $Z_{11} \neq Z_{22}$. The four units show an obvious bianisotropy that is caused by the strong dispersion of the units with constant phase differences. Our results clearly show that the broadband performance does require asymmetric structures due to the additional degrees of freedom offered by the asymmetry of the units. These results also suggest that the bianisotropy may have a broader impact on wave manipulations than most previous works had claimed, where the bianisotropy was primarily utilized for the directional wave control.

To further clarify the role of the bianisotropy, we also present the beam-regulation effect of the sector antenna when the acoustic wave is incident from the positive or opposite direction (see the Appendix). The design of the sector antenna is described in the following content (see Fig. 5).

In summary, the underlying mechanism of the broadband effect is rather complex and we can provide only a qualitative analysis. The resulting broadband effect is induced by the combination of both the internal resonance and the bianisotropy. As the bianisotropy is related to the unit symmetry, a stronger bianisotropy can increase the freedom of the cavity arrangement and may therefore enhance the internal resonance.

III. RESULTS AND DISCUSSIONS

Compared with the prosperous development of the coding metasurfaces in the community of electromagnetic and optical waves, the ACMs are obviously lacking awareness. However, the ACMs composed of limited kinds of coding units exhibit a high flexibility in acoustic wave control, and certain complicated functions include beam steering, wave bending, focusing, and random scattering,

etc. Furthermore, the BACMs can expand the manipulation flexibility in the frequency range, which is not attainable with narrowband ACMs.

A. Broadband sector-scanning sound antenna

The periodic variation in the frequency domain of the emission source will lead to the harmonic scattered-power distributions varying periodically with the frequency. The abovementioned frequency-angle-dependent features of the BACMs greatly improve the flexibility of the sound antenna. For example, we can design a sector-scanning antenna with a rapid frequency variation of the wave source, and the emission beams will fast scan a sector area periodically. This kind of frequency-angle scanning method can locate the azimuth of obstacles based on the echo frequency and it can further locate the distance by the echo time. Of note, the design of the acoustic antenna is a fixed coding sequence, and its scanning and echolocation mode does not depend on the reconfiguration of the coding units. Above all, the frequency-dependent broadband acoustic antenna designed by topology optimization can avoid the complexity of the reconstruction of the coding units by the traditional tunable approaches.

Abandoning the regulation method using the special dispersion relations, the BACMs can simply manipulate sound wave through different coding sequences composed of “0” and “1” (1-bit) or “00”, “01”, “10,” and “11” (2-bit). The sound-wave regulation principle of the BACMs can be explained by the traditional phased array antenna theory. To further quantitatively apply the above theory and method for describing the sound field, we assume that the square BACM contains $N \times N$ equal-sized units with the side length of L . The coding metamaterial is assembled by the distinct coding units, and the 2-bit coding metasurface is constructed by the four coding units “00”, “01”, “10,” and “11” exhibiting 0° , 90° , 180° , and 270° phase responses, respectively. Under the normal incidence of plane waves, the frequency-domain far-field pattern scattered by the BACMs can be expressed as [33]

$$f(\theta, \beta) = f_e(\theta, \beta) \sum_{m=1}^N \sum_{n=1}^N \exp \left(-j \left\{ \varphi(m, n) + \frac{2\pi f_{\text{peri}} L}{c_{\text{air}}} \sin \theta [(m - 0.5) \cos \beta + (n - 0.5) \sin \beta] \right\} \right), \quad (4)$$

where $\varphi(m, n)$ is the local scattering phase (0° , 90° , 180° , or 270°) of the m th ($m, n = 0, 1$) unit on the 2D plane of the coding metasurface. In addition, due to the regulating action of the metasurface, the far-field beam passing through the metasurface has a particular directivity. Here, we use θ and β to represent the elevation and

azimuth angles of the beam direction, respectively; $f_e(\theta, \beta)$ is the pattern function of a lattice; f_{peri} is the incidence frequency varying periodically; and c_{air} is the speed of sound in air. Consequently, the deflection angles of the far-field emission beams vary periodically with the frequency, and the scanning antenna within a sector area can

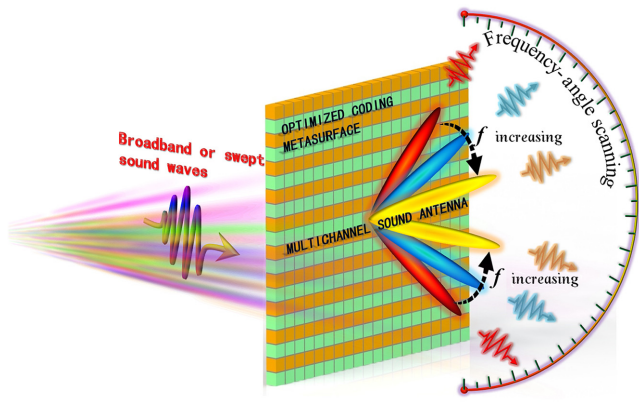


FIG. 4. Diagram of the far-field acoustic emission beam of the BACM having the simplest coding sequence with 010101.../010101..., where the deflection angle of the beam will decrease with the incidence frequency increasing.

be constructed. The emission beam of the sound antenna is related to the coding sequence. Figure 4 illustrates the far-field sound-pressure distributions for the simplest coding sequence with 010101.../010101..., where the deflection angle of the beam will decrease with the incidence frequency increasing. The above frequency-angle-dependent features of the BACMs greatly improve the flexibility of the wave regulation, which provides inspiration for fabricating multichannel sound antenna. By rapidly varying the frequency of the source, the emission beam will fast scan a sector area periodically, thereby locating obstacles according to the echo frequency. Moreover, as a splitter device, the BACMs can also separate the mixing waves by deflecting them into different directions according to the incidence frequencies. According to the generalized Snell law, the beam deflection angle is related to the phase gradient of the metasurface, and thus the refraction angle can be written as

$$\theta_t = \sin^{-1} \left[\frac{c_{\text{air}}}{2\pi f_{\text{peri}}} \cdot \frac{d\phi(y)}{dy} \right], \quad (5)$$

where $d\phi(y)/dy$ represents the phase-shift gradient along the coding sequence. Taking Fig. 5(e) as an example, the phase difference corresponding to the length of the four units in the y direction is 2π , so the phase gradient can be derived as $d\phi(y)/dy = 2\pi/4L$.

In this section, to show the validity of the broadband effects, most BACMs (except the checker-board pattern) are comprised of 20×20 units and the plane waves are normally illuminated on the incident port. To circumvent the narrowband limitation, our optimized BACMs can modulate the scattering beam in a continuously scanning angle. For far-field simulations, several ordinary 1-bit and 2-bit sequences are investigated in this section, and the broadband beam-emission results are presented in Fig. 5.

Since the topology optimization process is operated on the 2D plane, the flat topological configuration should be stretched into bricks [see Figs. 5(a)–5(d)], thereby assembling the three-dimensional (3D) BACMs. A metasurface consisting of an array with pure bits of “0” or “1” has no phase variety, and the refracted waves should vertically radiate from the BACM at broadband frequencies. The far-field patterns with different arrays of $\varphi(m, n)$ can be deduced from Eq. (4). For the simplest coding sequence of 0000.../0000..., the transmitted phase $\varphi(m, n)$ equals 0° for every unit, and the far-field pattern in Eq. (4) can be simplified as

$$|f_1(\theta, \beta)| = C_1 |\cos \psi_1 + \cos \psi_2| = 2C_1 \times \left| \cos \frac{\psi_1 + \psi_2}{2} \cos \frac{\psi_1 - \psi_2}{2} \right|, \quad (6)$$

where $\psi_1 = (\pi f_{\text{peri}} L / c_{\text{air}}) (\sin \theta \cos \beta + \sin \theta \sin \beta)$ and $\psi_2 = (\pi f_{\text{peri}} L / c_{\text{air}}) (-\sin \theta \cos \beta + \sin \theta \sin \beta)$, respectively. Obviously, when the sinusoidal functions reach 1, namely $|\cos[(\psi_1 + \psi_2)/2]| = |\cos[(\psi_1 - \psi_2)/2]| = 1$, the maximum scattering beam can be obtained at $\theta_1 = 0^\circ$ regardless of the incidence frequency f_{peri} . Consequently, the transmitted wave beam will radiate along the incidence direction. Furthermore, the similar far-field patterns for different coding sequences, for example, 010101.../010101... [see the results in Fig. 5(f)] and 101010.../010101... [see the results in Fig. 5(g)] can be also simplified, respectively, as

$$|f_2(\theta, \beta)| = C_2 |\sin \psi_1 + \sin \psi_2| = 2C_2 \times \left| \sin \frac{\psi_1 + \psi_2}{2} \cos \frac{\psi_1 - \psi_2}{2} \right|, \quad (7)$$

$$|f_3(\theta, \beta)| = C_3 |\cos \psi_1 - \cos \psi_2| = 2C_3 \times \left| \sin \frac{\psi_1 + \psi_2}{2} \sin \frac{\psi_1 - \psi_2}{2} \right|. \quad (8)$$

The maximum points for sequence 010101.../010101... can also be derived from Eq. (4) as $\beta_2 = 90^\circ$ and 270° , and $\theta_2 = \sin^{-1}(c_{\text{air}}/4Lf_{\text{peri}})$, while the corresponding ones $\beta_3 = 45^\circ, 135^\circ, 225^\circ$, and 315° , and $\theta_3 = \sin^{-1}(c_{\text{air}}/3\sqrt{2}Lf_{\text{peri}})$ for sequence 101010.../010101.... In order to locate the refraction angle within a reasonable range of 0° – 90° throughout the broadband frequency region, each code number consists of two units for sequence 010101.../010101... and three units for sequence 101010.../010101.... Therefore, the incident plane wave is scattered into two or four beam branches, and the deflection angles vary continuously depending on the periodic frequency, namely $\theta_2 \in (27.7^\circ, 56.8^\circ)$ for $f_{\text{peri}} \in (2500\text{Hz}, 4500\text{Hz})$, and $\theta_3 \in (26.6^\circ, 46.9^\circ)$ for $f_{\text{peri}} \in (2700\text{Hz}, 4400\text{Hz})$. It should be pointed out that, in order to make the refraction angle θ_3 locate in a reasonable range within 0° – 90° , we adopt the overall dimensions of

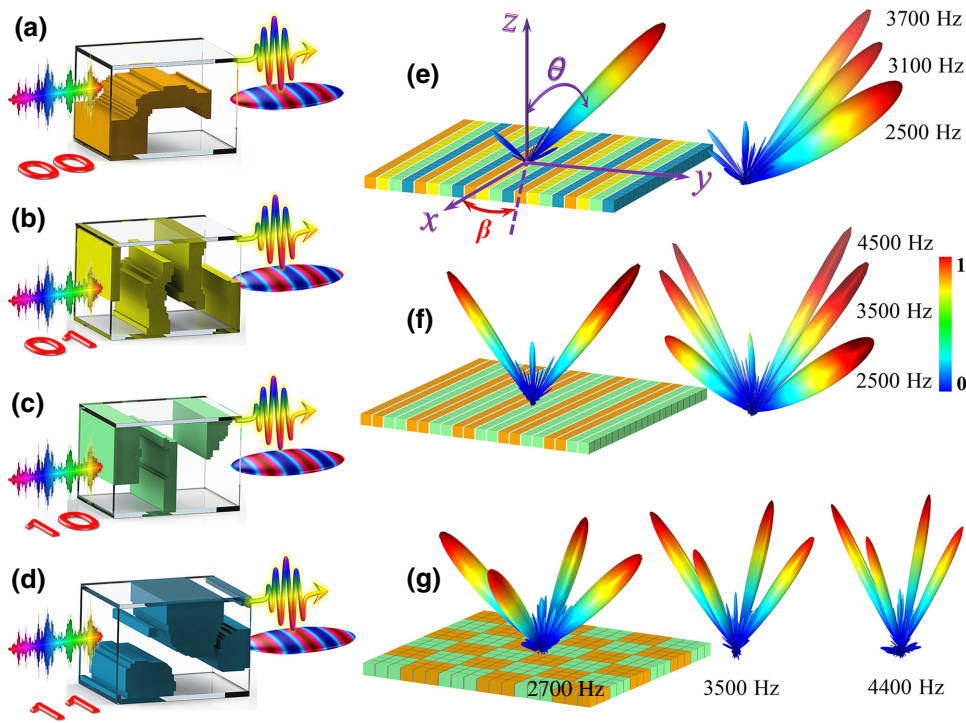


FIG. 5. Detailed structures of the 3D units and the far-field beam-emission results for different coding sequences. (a)–(d) Detailed structures of the 3D-printed four units and their phase-delay schematics. (e) The broadband single-beam emission results of the 2-bit BACM with the coding sequence of 00 01 10 11.../00 01 10 11... (f) and (g) The far-field patterns for the 1-bit BACMs with different coding sequences, namely 010101.../010101... in (f) and 101010.../010101... in (e), and the incident plane wave is scattered into two or four beam branches. The beam colors in (e)–(g) represent the normalized pressure amplitude of the far-field patterns.

18×18 units in the checker-board pattern with each code number consisting of a supercell with 3×3 units. In addition, constructing the single-beam scanning antenna by the 2-bit BACMs is feasible. The broadband results are presented in Fig. 5(e). With a unidirectional phase gradient, the 2-bit sequence 00 01 10 11.../00 01 10 11... has a single branch effect, and the refracted angle can be derived from Eq. (5) as $\theta_4 = \sin^{-1}(c_{\text{air}}/4Lf_{\text{peri}})$, which gives rise to a single-beam scanning angle of $\theta_4 \in (34.4^\circ, 56.8^\circ)$ for $f_{\text{peri}} \in (2500\text{Hz}, 3700\text{Hz})$.

As aforementioned, the sequences of the partial BACMs are essentially one dimensional (1D), such as 010101.../010101... in Fig. 5(f) and the 2-bit sequence of 00 01 10 11.../00 01 10 11... in Fig. 5(e). Thus, the 2D coding array can be compressed to a 1D strip sequence, and the numerical simulation as well as the experimental operation process will be significantly simplified. The experiments of the above 1D BACMs are conducted in a waveguide system, which consists of two hard waveguide plates with the surrounding border being filled with sound-absorbing sponge, see Fig. 6(a). A row of loudspeakers located on the incident part of the structure works as a plane-wave source, and the testing microphone on the other part will scan the reconstructed sound field point by point. In conjunction with the reference microphone, we can measure the pressure amplitude and phase distribution. Then, based on the discrete data we can plot the 2D sound-field profile. And subsequently the beam-emission direction can be evaluated by the tilt angle of the wave front. To reduce the experimental test region, we adopt 14 units for the 1-bit BACM with the sequence of

010101...; and another 2-bit sequence of 00 01 10 11... composes a 1D BACM with 16 units having four coding periods, as shown in Fig. 6(b). In the full-field numerical simulation for the sector-scanning acoustic antenna, each code number consists of a supercell having two units. As for sequence of 010101..., we have $\theta_2 \in (27.7^\circ, 56.8^\circ)$ for $f_{\text{peri}} \in (2500\text{Hz}, 4500\text{Hz})$. The simulated and experimental results are presented in Figs. 6(c) and 6(d). As shown in the figures, the 1-bit coding metasurface can also be regarded as a beam splitter that can separate the incident sound waves into two waves with a certain angle. In addition, the numerical simulation and the experimental verification of a 2-bit single-beam broadband scanning antenna are also carried out, see Figs. 6(e) and 6(f).

To quantitatively describe the refractive directions, we further analyze the beam-emission properties of the sound fields by the Fourier-transform method [49]. First, we extract the real and imaginary parts of the pressure field along the line above the device, as shown by the dashed line in Fig. 6(b), and then apply the Fourier transform to calculate the diffraction orders based on the data. Specifically, for the normal incidence direction of $\theta_i = 0^\circ$, the diffraction orders are calibrated by the proportion factor k_x/k_0 , where k_x is the tangential component of the diffracted wave vector, such that the corresponding refraction angle of the normally incident waves can be found from $\theta_r = \sin^{-1}(k_x/k_0)$. For all beam-emission results, most of the acoustic energy is localized between the -1 order and $+1$ order (from -90° to 90°), while the other diffraction orders are almost completely suppressed. Furthermore, the wave-vector component perpendicular to the

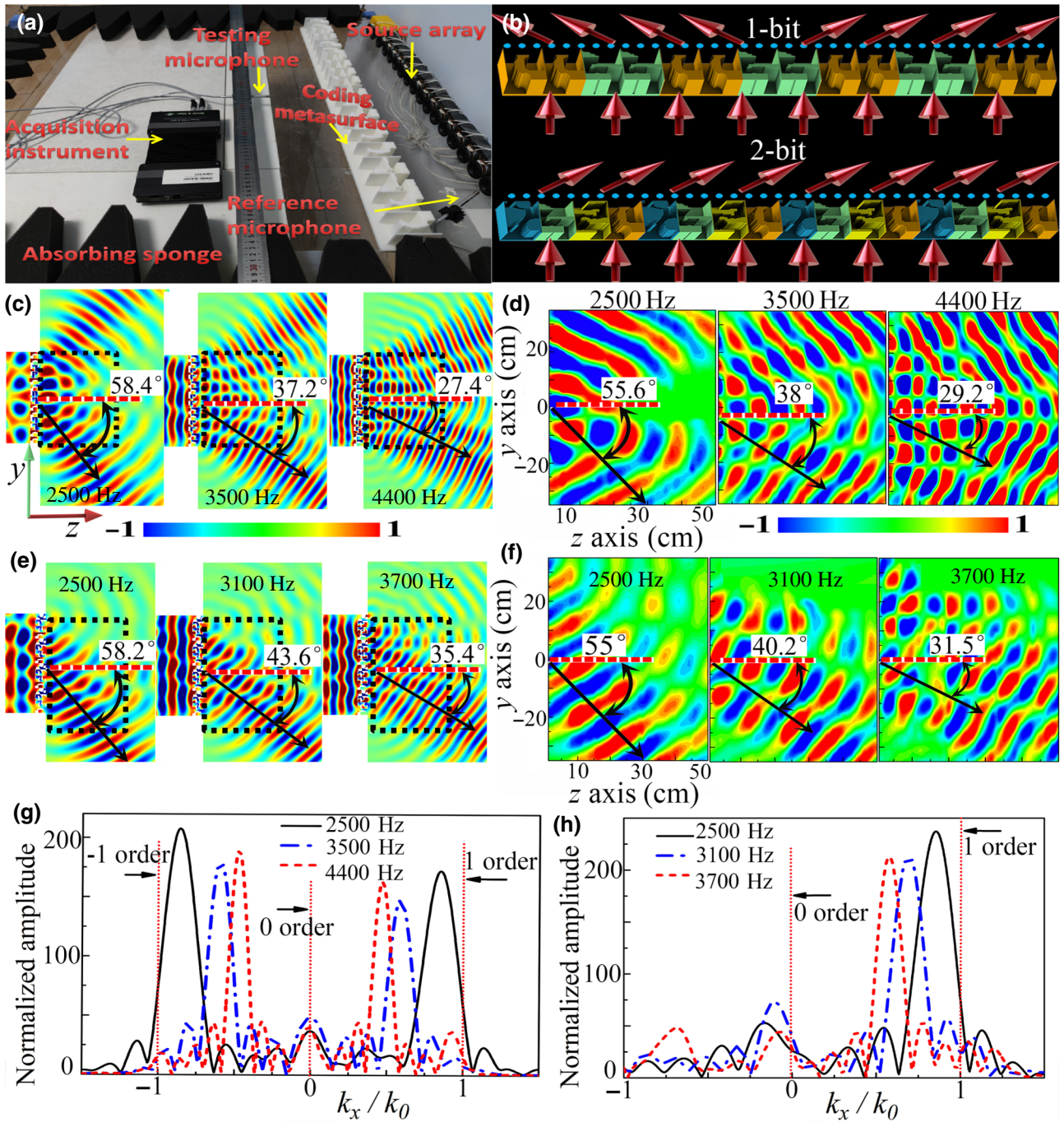


FIG. 6. Numerical and experimental verifications of the 1-bit and 2-bit 1D broadband BACMs. (a) The waveguide experiment system for the 1D BACMs. (b) The schematic diagram of the 1-bit and 2-bit 1D BACMs with the coding sequences of 010101.../010101... and 00 01 10 11.../00 01 10 11.... (c)–(d) Simulated and experimental results of the 1-bit sequence at the frequencies of 2500, 3500, and 4400 Hz. The corresponding double-beam deflection angles are signed in the figure. (e)–(f) Numerical simulation and experimental verification of the 2-bit single-beam broadband BACM at the frequencies of 2500, 3100, and 3700 Hz. The counterpart beam deflection angles are signed in the figure. (g)–(h) The spatial Fourier transform of the simulated near-field pressure along the 1-bit and 2-bit BACMs. Most of the energy is localized between the -1 and $+1$ orders, and the locations of the energy peaks are used to obtain the beam-deflection-angle results.

BACMs has the imaginary value of $k_y = i\sqrt{k_x^2 - k_0^2}$ in the case of $k_x \geq k_0$, which means that the evanescent wave

modes arise. To validate the broadband frequency-angle scanning property, we further study the Fourier-transform results at the representative frequencies of 2500, 3500, and

4400 Hz corresponding to the sequence of 010101. . . . The different diffraction orders presented in Fig. 6(g) are clearly visible; and the energy peaks within $(-1,1)$ lead to the beam-deflection-angle results within 27.4° – 58.4° , which is close to the theoretical value of $\theta_2 \in (27.7^\circ, 56.8^\circ)$. We also conduct the Fourier transform to the pressure field along the line above the 2-bit BACM at the frequencies of 2500, 3100, and 3700 Hz. For the single-beam emission results, most of the energy is localized between the 0 order and +1 order, as shown in Fig. 6(h). The beam-deflection angles are obtained by positioning all the peak locations based on the corresponding frequencies. The angle results of 58.2° (2500 Hz), 43.6° (3100 Hz), 35.4° (3700 Hz) are in fairly good agreement with the theoretically predicted results of $\theta_4 \in (34.4^\circ, 56.8^\circ)$.

The above results are based on several common coding sequences for far-field beams' radiation. By introducing broadband frequency-angle scanning technology, the BACMs with a rapid angle-scanning ability can be deduced. In the following part, we introduce the convolution concept, study more complex beam-scanning features of the BACMs, and further clarify their flexible wave-beam control performance.

Broadband scanning antenna have the ability to shape the plane waves into targeted complicated beams, which will greatly improve its detection functions and extend the scope of its applications. Fortunately, by performing convolution operations on the BACMs, we can make

more useful explorations on multibeam scanning antenna [50]. The concept implies that if employing a convolution between a spectrum function $f(\omega)$ and an impulse function $\delta(\omega - \omega_0)$, the spectrum function will shift ω_0 in the frequency domain without distortion. The equivalent effect between the convolution in the frequency domain and the multiplication in the corresponding time domain can be described by

$$f(t) \cdot e^{i\omega_0 t} \xleftrightarrow{\text{FFT}} f(\omega) * \delta(\omega - \omega_0) = f(\omega - \omega_0). \quad (9)$$

Since the acoustic field on the coding metasurface and its corresponding far-field scattering pattern are a Fourier-transform pair, the convolution operation can be introduced to design the coding metasurfaces. The principle of the scattering-pattern shift can be similarly described by

$$\begin{aligned} P(x_\lambda) \cdot e^{ix_\lambda \sin \theta_0} &\xleftrightarrow{\text{FFT}} P(\sin \theta) * \delta(\sin \theta - \sin \theta_0) \\ &= P(\sin \theta - \sin \theta_0), \end{aligned} \quad (10)$$

where $x_\lambda = x/\lambda$; and θ is the angle with respect to the incidence direction. The above formula means that the multiplication between a coding pattern of $P(x_\lambda)$ and the gradient coding sequence of $e^{ix_\lambda \sin \theta_0}$ will bring an angular deviation to the far-field acoustic beam $P(\sin \theta)$ with a specific value of $\sin \theta_0$. It should be noted here that the convolution idea gives us a design perspective for coding

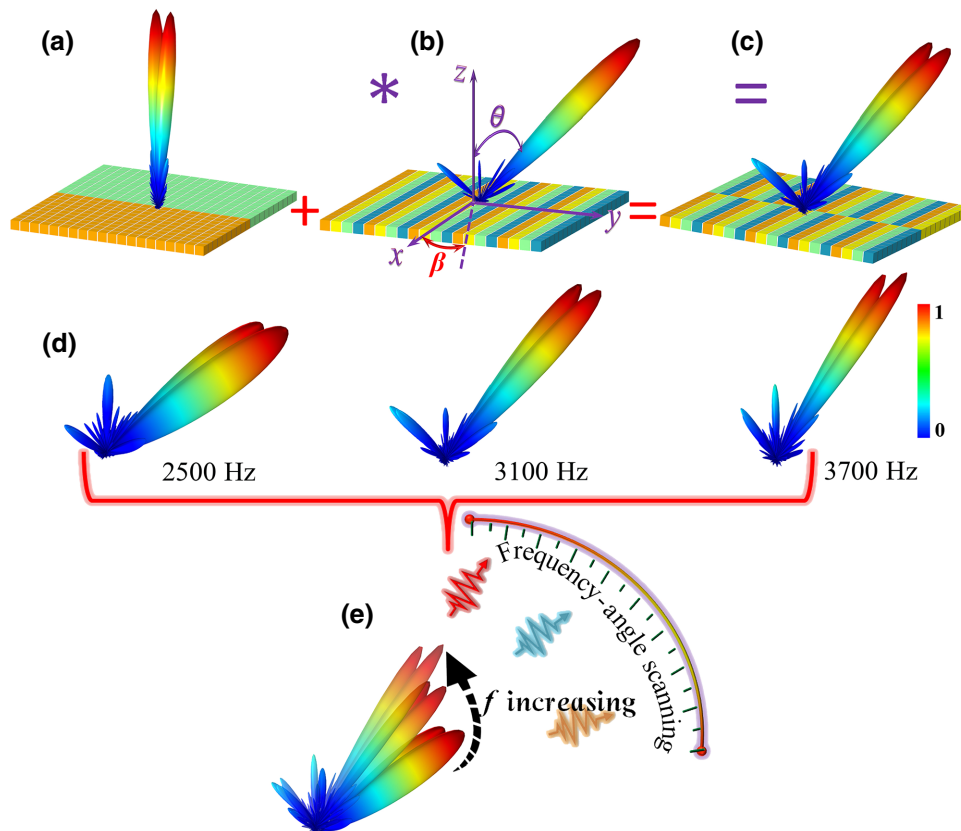


FIG. 7. A double-beam scanning acoustic antenna based on the convolution method. (a)–(c) The convolution implementation process of the double-beam deflection case. The multiplication of the 1-bit symmetrically shaped coding pattern in (a) and the 2-bit gradient coding sequence in (b) allows the BACM in (c) to manipulate the deviation angle of the scanning beams flexibly. (d) The simulated double-beam deflection results at the frequencies of 2500, 3100, and 3700 Hz. (e) The broadband beams' deflection diagram.

metasurfaces to realize a flexible control of the radiation beams to arbitrarily desired directions.

In this section, we employ the 2-bit BACMs to demonstrate how the convolution concept is used to construct a broadband multibeam scanning acoustic antenna. Unlike the previous simple “0” and “1” sequences, the multiplication of the 1-bit coding pattern with known scattering beams, and the 2-bit gradient coding sequence allows the BACMs to manipulate the deviation angle of the scanning beams flexibly with significantly reduced computational complexity. For instance, if the symmetrically shaped 1-bit coding pattern in Fig. 7(a) is multiplied by a 2-bit gradient sequence such as “00 01 10 11...” in Fig. 7(b), the originally split two main beams will deviate from the x - z plane with an angle depending on the frequency. Consequently, we can easily construct a double-beam scanning acoustic antenna [Fig. 7(c)] having a smart frequency-angle sensitivity. The broadband far-field acoustic scattered-power distributions are presented in Fig. 7(d), where the swept angle varies periodically with the cyclically changing frequency. The deviated angles of the convolution results will follow the 2-bit sequence 00 01 10 11.../00 01 10 11... having $\theta = \sin^{-1}(c_{\text{air}}/4Lf_{\text{peri}})$; and the corresponding values in Fig. 7(e) is $\theta \in (34.4^\circ, 56.8^\circ)$ within the frequency range of $f_{\text{peri}} \in (2500 \text{ Hz}, 3700 \text{ Hz})$.

Moreover, this operation approach can be extended to a lot of other analogous complex wave-beam manipulations. As examples, we also demonstrate the sector-scanning properties of the triple-beam antenna created by the banded coding sequences and the multibeam cluster antenna generated by the cross-shaped coding pattern, which are presented in Figs. 8(a) and 8(d), respectively. The convolution between the original triple-beam coding pattern in Fig. 8(a) and the 2-bit coding sequence in Fig. 8(b) will generate a broadband deviated triple-beam coding pattern. The broadband property is efficient between 2500 and 3700 Hz, within which the emission angle varies in the range $\theta \in (34.4^\circ, 56.8^\circ)$. Similar to the triple-beam sound antenna, a beam cluster having five beams generated by a cross-shaped coding pattern is presented in Fig. 8(d), and its convolution with the 2-bit gradient sequence will also deflect the emission wave beams with a specific angle dependent on the frequency. From the simulation results in Fig. 8(g), the elevation angle is $\theta \in (35.6^\circ, 48.4^\circ)$ in the operation frequency range of $f_{\text{peri}} \in (2800 \text{ Hz}, 3600 \text{ Hz})$. The idea of combining both of the BACMs and the Fourier transform provides us another degree of freedom in designing complex-beam scanning antennas. All of the sector-scanning antennas afford us a sufficient optionality in the field of sound detection. Meanwhile, the

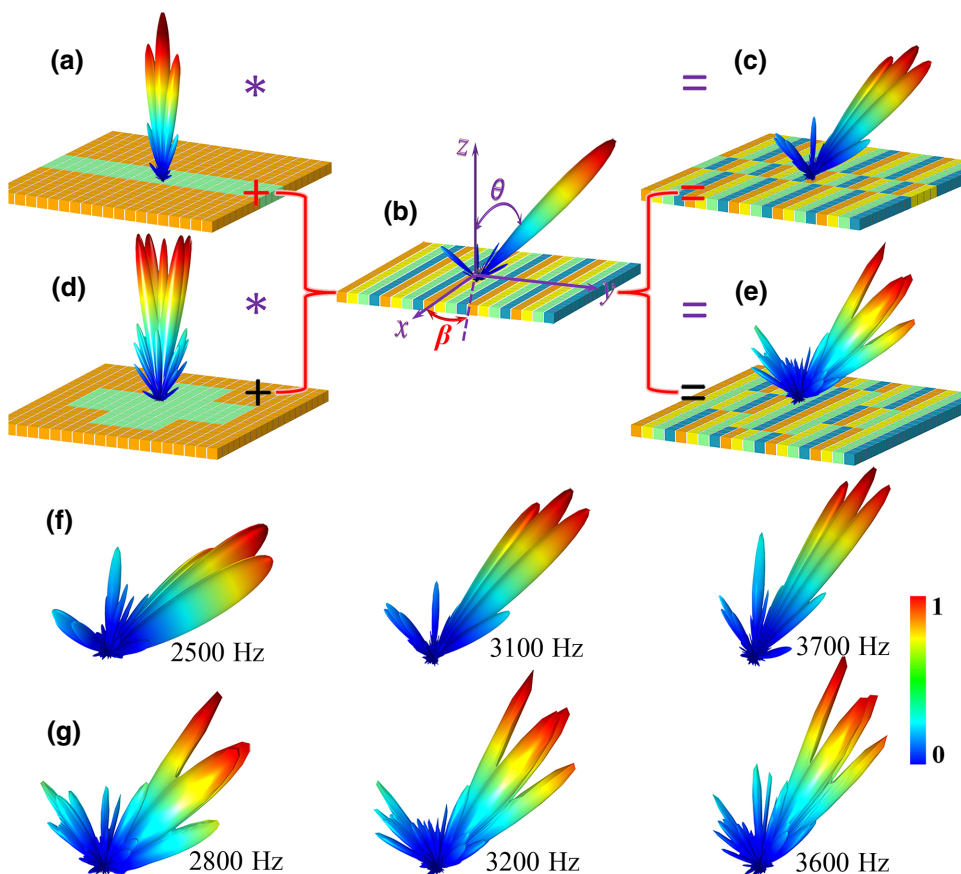


FIG. 8. The triple-beam and the multibeam cluster antennas generated by the banded and cross-shaped coding sequences. (a)–(e) The convolution implementation process to achieve the deflection of the triple-beam and multibeam clusters. (f)–(g) The broadband beams’ deflection results, where (f) is the simulated far-field results at frequencies of 2500, 3100, and 3700 Hz, and (g) is the corresponding multi-beam deflections at 2800, 3200, and 3600 Hz.

innovative frequency-angle locating method has the advantages of stability, rapidness, and accuracy.

B. Broadband coding Fresnel lens

Compared with the previously proposed ACMs, the present BACMs can also bring alternative control flexibility to the Fresnel lens in terms of broadband frequency. Two different types of the 0 and 1 coding units can build various focusing lenses and consequently realize the customized focusing performance. Here we propose a pluggable mortise and tenon way to refactor the broadband Fresnel lens, see Fig. 9(a). Although this refactoring method is not automatically controlled, its broadband characteristics enhance the engineering applicability. When manufacturing the lens by the 3D printing technology, the baseboard and coding units are separately printed. Moreover, we reserve a tenon on the partition plates between the units, whereas a matching mortise is cut on the baseboard. This kind of easy-plug design can reassemble the location of the coding units by hand and further reset the Fresnel lens, hence achieving flexible focusing results in a broadband scope. A thin flat Fresnel lens consisting of Fresnel zones is similar to the effect of the focusing lens. Through a proper configuration of the reverse phase bits of 0 or 1, the Fresnel lens can concentrate the sound waves at the desired focal point. Consistent with the abovementioned fact, in Fig. 9(a) the orange area indicates the zones composed of the bit “0,” and the green area indicates the zones composed of the bit “1.” In order to make the sound waves have constructive interference at the focal point, the wave-path difference between the adjacent Fresnel zones should satisfy

$$l_{i+1} - l_i = \frac{\lambda}{2}, \quad (11)$$

where $\lambda = c_{\text{air}}/f$ is the wavelength of the focal frequency f ; and $l_i = \sqrt{z_f^2 + r_i^2}$ ($i = 1, 2, 3 \dots$) is the length of the wave path from the i th zone to the focal point, with z_f being the focal length and r_i denoting the horizontal distance of the midpoint of the i th zone to the center of the lens, see Fig. 9(b). For the central zone, we have $r_1 = 0$ and $l_1 = z_f$. From Eq. (11), we can locate the midpoint of the $(i+1)$ th zone as [7]

$$r_{i+1} = \sqrt{(\lambda/2 + \sqrt{z_f^2 + r_i^2})^2 - z_f^2}. \quad (12)$$

Once the frequency f and the focal length z_f are established, then the Fresnel zones composed of the bits 0 or 1 are also settled. Because each zone consists of integer coding units, and the side length of the coding bit is $L = 0.042$ m, it is very hard to make the Fresnel zones meet Eq. (12) precisely without introducing any solid fillers between

the zones. Therefore, in this section, the size condition of each zone is only approximately satisfied, and a limited number of 20 bits are used to build the Fresnel lens. We take the focal length $z_f = 0.3$ m and the frequency 3000 Hz ($\lambda = 0.114$ m) as an example to show how to ascertain the 0 or 1 coding number in every Fresnel zone. When the abovementioned numbers are finally assigned to the parameters of Eq. (12), the zones' midpoints are evaluated as $r_1 = 0$, $r_2 = 0.1938$ m, $r_3 = 0.2858$ m, and $r_4 = 0.3637$ m. As a result, the coding-unit numbers from the center of the lens to the edge are 4-2-2-2, respectively, and the coding sequence of 0011001111111001100 approximately satisfies the focusing requirement. As for the other focusing conditions, the coding sequences are marked in Fig. 9. To highlight the broadband features, we adopt the reconfiguration method to build the BACMs. In theory, the sound focusing with any focal length in the broadband of $f \in (2500 \text{ Hz}, 4000 \text{ Hz})$ can be obtained by reconstructing the coding units in each Fresnel zone.

Below we exemplify Fresnel lenses with varying coding sequences that present specific focal effects, such as a series of the same focal length at different frequencies, see the experimental results in Fig. 9(c) and the simulation results in Fig. 9(d). The sound fields with the same focal length of 0.3 m at the frequencies of 2500, 3000, 3500, and 4000 Hz show a high degree of consistency in the focal location; and the broadband experimental results in Fig. 9(c) are close to the simulation results in Fig. 9(d). In order to further clarify the efficiency of the focusing property, the normalized longitudinal pressure fields at the focal spot along the z direction ($x = 0$) corresponding to Fig. 9(d) are shown in Fig. 9(f). In addition to the focusing effect at different frequencies with the same position, we also demonstrate the focusing results at the same frequency (3500 Hz) but at different positions (0.1 m, 0.2 m, 0.3 m, 0.4 m), as shown in Fig. 9(e). The pressure amplitude across the focal spot along the z direction in Fig. 9(g) also confirms that the required focal lengths obtained by the numerical simulation and the experimental measurement are correct and in fairly good agreement. Figures 9(c)–9(e) all show a sharp focal spot that is higher than 2 times of the pressure amplitude of the incident plane wave.

C. Broadband acoustic diffusion

Through combining the two unit cells with out-of-phase responses, the BACMs can achieve a broadband diffusion scattering and its broadband validity also does not require a reconfiguration of the units. It is worth mentioning that the broadband-transmission-type diffusion-scattering design is different from the previous reflective type, which is beneficial to transform the internal sound field into the external diffusion one. This transmission design has potential applications including the automatic antenna control and the reduction of the acoustic radar cross section (RCS), as well

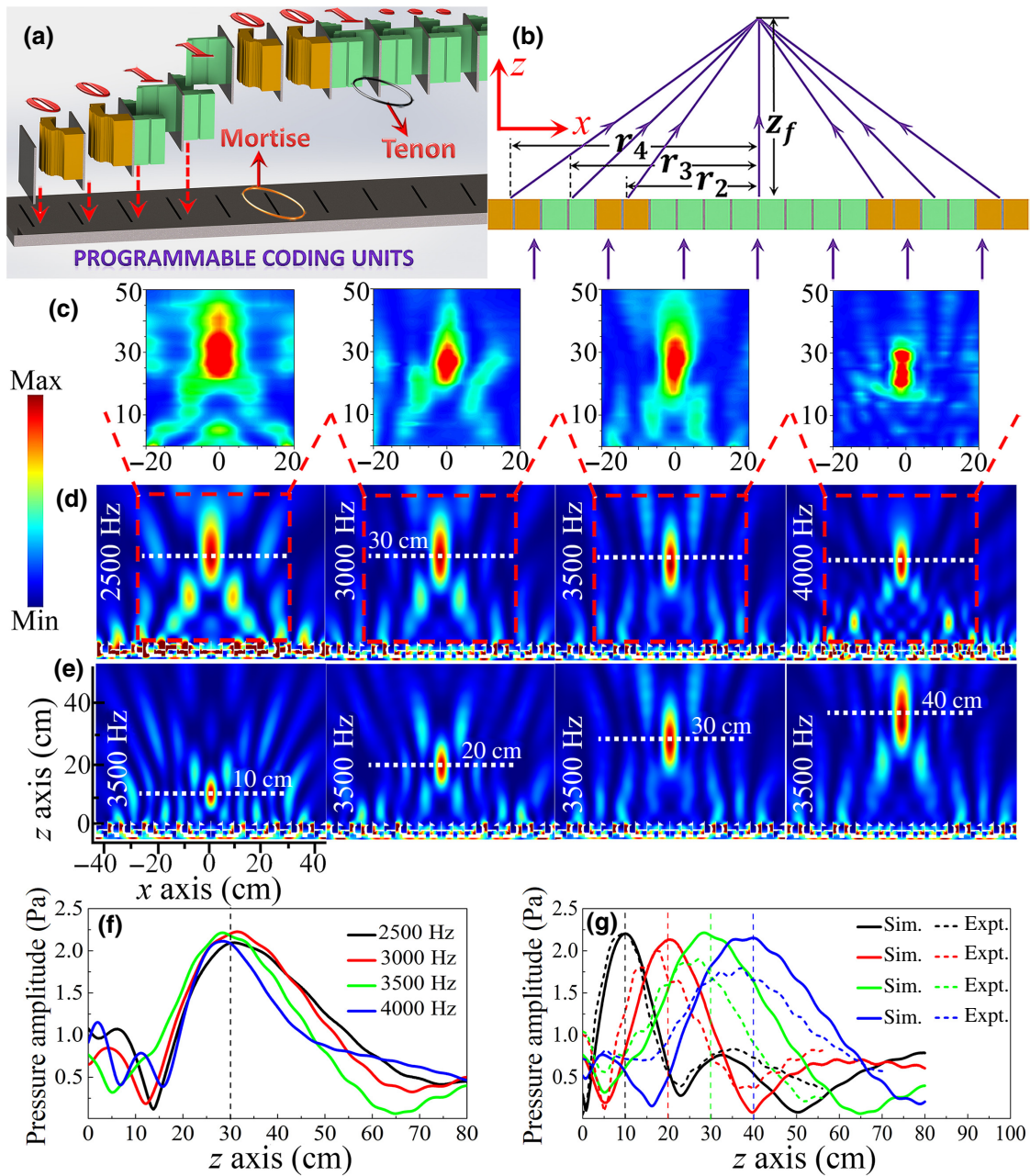


FIG. 9. Numerical simulation and experimental study of the broadband coding metasurfaces with the focusing properties. (a) and (b) Schematic diagram of a reconfigurable 1D coding metasurface and its focusing effect. (c) and (d) The experimental results in (c) and the simulation results in (d) show a series of the focusing effects with the same focal length of 0.3 m at the frequencies of 2500 Hz for the sequence of 0110011111111100110, 3000 Hz for the sequence of 00110011111111001100, 3500 Hz for the sequence of 10011001111110011001, and 4000 Hz for the sequence of 01011001111110011010. (e) The simulated focusing results at the frequency of 3500 Hz but different focal points (0.1 m for the sequence of 10010110111101101001, 0.2 m for the sequence of 0100110111110110010, 0.3 m for the sequence of 10011001111110011001, and 0.4 m for the sequence of 0011001111111001100). (f) The normalized longitudinal pressure fields at the focal spot along the z direction ($x = 0$) corresponding to (d). (g) The simulated and experimental pressure fields across the focal spot in (e).

as the sound-field shaping in reverberating scenarios. As a useful application, the reduction of the acoustic RCS based on the BACMs aims to reduce the far-field detectability of the noise sources. In fact, different cloaking strategies

such as underwater cloaking using pentamode metamaterials force waves to bend around the target [51]; while the sound-absorption method uses an anechoic cover composed of a sound sponge or thin metamaterial [52]. But

here, we propose a coding method to reduce the acoustic RCS. By an adequate spatial arrangement of the coding units, the acoustic radiation energy is redirected to all directions. Compared with the reflective coding metasurfaces whose diffusion design can reduce the acoustic active detection, the transmission BACMs can refract the broadband acoustic waves uniformly in all possible directions, thereby leading to an obvious acoustic RCS reduction in both single and multibase passive detection.

Here, we introduce the pair of the out-of-phase units with the numbers of “01” and “11” in Fig. 2 as the coding units of the acoustic diffusion metasurface. For simplicity, the two units are also marked as the “0” or “1”. Furthermore, to specifically illustrate the acoustic diffusion phenomena, we consider a square BACM containing $N \times N$ equal-sized supercells with the side length of D . The supercells labeled with “0” or “1” are composed of $M \times M$ units, therefore, we get the side length of $D = ML$. Relative to a total reflection on the acoustic hard boundary or a plane-wave source radiation, the RCS reduction brought by the BACMs can be derived as [25]

$$S = \frac{\lambda^2}{4\pi N^2 D^2} \text{Max}_{\theta, \varphi} [\text{Dir}(\theta, \beta)], \quad (13)$$

where $\lambda \in [0.0858 \text{ m}, 0.149 \text{ m}]$ is the broadband wavelength related to the frequencies from 2300 to 4000 Hz. In addition, the directivity function $\text{Dir}(\theta, \beta)$ of the metasurface can be written as

$$\text{Dir}(\theta, \beta) = 4\pi |f(\theta, \beta)|^2 / \int_0^{2\pi} \int_0^{\pi/2} |f(\theta, \beta)|^2 \sin \theta d\theta d\beta, \quad (14)$$

where $f(\theta, \beta)$ is identified as the far-field function, which is equal to the pattern function of a coding bit made of the supercell, i.e., $f(\theta, \beta) = f_e(\theta, \beta)$. In this part, our aim is to suitably assemble the coding sequences to minimize the metasurface directivity function $\text{Dir}(\theta, \beta)$ with respect to θ and β , so that the transmitted waves will be radiated in all possible directions uniformly.

The coding sequences having the best acoustic RCS reduction should be achieved by optimization method. Several optimization options have been put forward to minimize the electromagnetic RCS, e.g., the particle-swarm [53], the simulated annealing [54], and the sub-optimal methods [33]. Here, we particularly mention the mature optimization strategies in Refs. [25,33] and give some examples of the acoustic diffusion analogy for comparison. In our designs, the supercell size D is fixed as λ so that the code sequences along the horizontal and vertical directions are the same. Fortunately, the broadband character of our optimized out-of-phase units still prevails in designing the broadband acoustic diffusion metasurface, because the RCS reduction remains relatively insensitive

TABLE I. P_v -type GRS polynomial coding sequences with different v .

v	N	Coding sequence
2	4	1110
3	8	11101101
4	16	1110110111100010
5	32	11101101111000101110110100011101

when D/λ varies from 0.6 to 3.0 [25]. In order to ensure the approximate consistency between the broadband wavelength and the supercell size, we assign the supercell with 3×3 units, that is, $D = 0.126 \text{ m}$; and we have $D = \lambda$ at the frequency of 2722 Hz. Following the suboptimal design strategy, we introduce the Golay-Rudin-Shapiro (GRS) polynomials to construct the P_v -type GRS polynomial coding sequence that is generated rather straightforwardly. It can be verified that the number of the generated polynomial coding bits can be written as $N = 2^v$, where v is a variable value. Another advantage of the suboptimal method is that with the increase of the optimization scale, the requirements on the computing resources do not increase significantly. The abovementioned GRS supercell coding sequences with different v are listed in Table I.

Without loss of generality, in the following numerical and experimental investigations, we adopt $v = 3$ and the coding number $N = 8$ to further explore the broadband diffusion effect. The relative coding sequence containing the above eight “0” or “1” bits is “11101101” as shown in Table I. Because both of the x and y directions have the same coding sequence under the certain prerequisites in this section, the 1D coding sequence can be simply extended to the 2D plane coding sequence with its schematic diagram being displayed in Fig. 10(b). Under the irradiation of the vertical sound waves, the above BACM increases the uniformity of the scattered sound energy, thus reducing the directivity of the radiation beam. The inset of Fig. 10(b) shows the detailed structures of the two 3×3 units, with the two colors representing different bits. The experimental setup in Fig. 10(a) contains the homogeneous source array, 3D-printed testing sample, 1/8-inch microphone, automatic scanning equipment, and surrounding absorbing sponge. From the simulated far-field acoustic scattering results, it can be found that the BACM can achieve a 10–16 dB acoustic RCS reduction in the design broadband frequency range from 2300 to 4000 Hz. Figure 9(c) shows the simulated far-field RCS patterns of the BACM at three discrete frequencies, namely 2500, 3100, and 3700 Hz. As shown in the figure, the RCSs are always lower than -10 dB , and in all directions the scattered acoustic fields are suppressed at relatively low levels. According to the energy conservation principle, the acoustic wide-angle scattering can reduce the radiation energy in a single direction as a consequence.

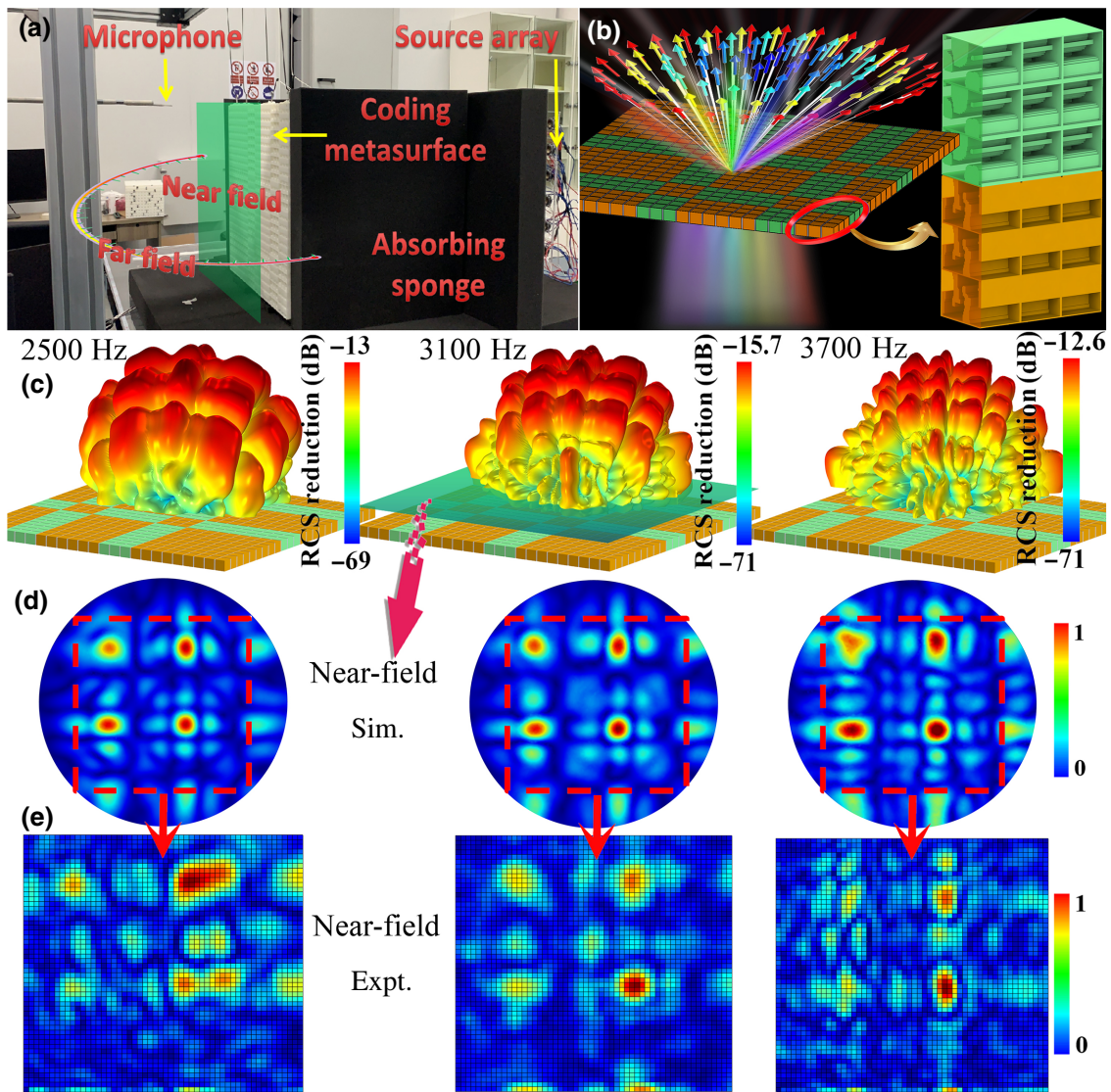


FIG. 10. Numerical simulation and experimental study of the broadband acoustic diffusion properties. (a) The experimental setup for the 3D acoustic field testing. (b) Schematic diagram of the broadband diffusion metasurface and the detail structure of the coding supercells. (c) Simulated far-field RCS patterns of the BACM at three discrete frequencies of 2500 Hz, 3100 Hz and 3700 Hz. (d) and (e) The near-field acoustic simulation and scanning test results.

At the same time, the near-field acoustic simulation and the scanning test results in Figs. 10(d) and 10(e) show multiple energy speckles, which further indicates the far-field diffusion property.

In addition to the near-field plane test, we also give the far-field experimental results in Fig. 11. The inset arc curve with a radius of 1 m in the schematic diagram of Fig. 10(a) is the moving trajectory of the microphone in the far-field test. These polar plots in Figs. 11(a)–11(c) show a high degree of agreement between the simulation and experimental results. As shown in the figures, the sound energy distribution is relatively uniform over the test range of 180° . Comparing the far-field RCSs for the uniform bit arrangement and the diffusion coding sequence, the

simulation and experimental RCS reduction data are presented in Fig. 10(d). Obviously, more than -10 dB RCS reduction is achieved between 2300 and 4000 Hz and the maximum reduction even reaches -16 dB. The above experimental results are proved to be robust by repeated measurements.

IV. NUMERICAL SIMULATIONS

Throughout the paper, the full-field wave simulations are performed by using COMSOL Multiphysics 5.3 with the pressure acoustics module. The background medium is air and the solid portion of the BACM is considered as an acoustically hard material; and therefore, the

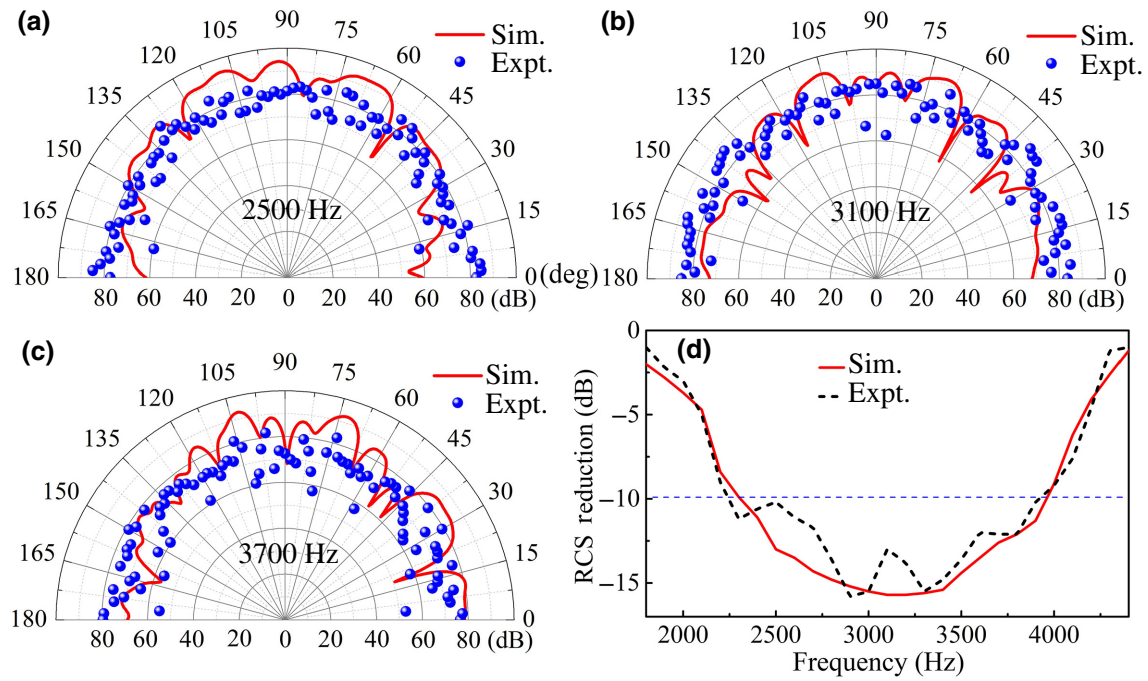


FIG. 11. Numerical and experimental results of the far-field broadband acoustic diffusion properties. (a)–(c) The far-field simulation and experimental results at three different frequencies of 2500, 3100, and 3700 Hz. During the test, the microphone is scanning the points on the semicircle arc around the BACM and the radius of the arc is 1 m. (d) The broadband simulation and experimental far-field RCS reduction data.

acoustic hard boundaries are introduced on the surface of the solid structure. To eliminate the reflected waves on the outer boundaries of the computational domain, the plane-wave radiation boundary condition is adopted. The incident plane wave is excited on the source port. To consider the far-field distribution of the scattered wave beams, we use the exterior field boundaries on the surfaces of the domain, which allows the calculation and visualization of the pressure field outside the computational domain at any distance including the pressure amplitude and phase.

V. EXPERIMENTAL VALIDATION

The BACM samples having the functions of the broadband acoustic wave scanning, focusing, and diffusion are 3D printed by the printer UnionTech Lite800HD (Company: Wenext) with a printing resolution of 200 μm . The printing material is the low-viscosity photosensitive resin with the elastic modulus about 2500 MPa and the mass density of 1250 kg/m^3 . The waveguide test scheme is adopted in the experiments of the scanning-beam antenna and focusing. To characterize the acoustic field, the 1/8-inch microphone (type 4138-A-015) is connected with the B&K data acquisition device (type 3160-A-042), which measures the acoustic pressure by moving it on the plane within the waveguide. The surrounding boundaries are filled with a sound-absorbing sponge to reduce the impact

of the reflected sound waves. In the 1D experimental test, the microphone scanning area is $70 \times 50 \text{ cm}^2$ for the single- or double-beam acoustic antenna. As for the broadband diffusion test, we use automatic scanning equipment to control the microphone for the far-field sound-pressure level and the near-field sound-pressure scanning detection. In the experiment, a 6×6 source array is used to generate incident plane waves.

VI. CONCLUSIONS

In this paper, we propose an optimization-based design method and its experimental validation to construct broadband acoustic coding metasurfaces whose units exhibit a fixed phase difference in a broadband frequency range. The optimal design of the metamaterials can overcome the unpredictability of the unit cell's dispersion and then achieve customized dispersion characteristics that meet the rigorous requirements. For broadband coding metasurface, the units must support specific dispersion. For example, the refractive index of the units varies nonlinearly with the increase of frequency that is called customized dispersion. Utilizing the optimization strategy, we design the 1-bit coding units with out-of-phase responses and the 2-bit coding units with four phase shifts of 0° , 90° , 180° , and 270° . The above phase differences result in a broadband stability. The broadband customized dispersions can be qualitatively explained by a combination

of the internal resonances and the bianisotropy effect. Because the far-field scattering-beam angles are dependent on the frequencies, so by making the convolution operations on the metasurfaces, we explore the single- or multibeam acoustic scanning antennas. Furthermore, through refactoring the out-of phase coding bits, we introduce a flexibility in customized focusing to the coding Fresnel lens. The pluggable unit is simple and feasible. The experimental study validates the effectiveness of this regulation mechanism. In addition, the optimized coding sequences can redirect the transmitted waves to all possible directions, and the scattered energies in all directions are suppressed to low levels. The simulation and experimental results clearly demonstrate the broadband acoustic RCS reduction properties.

The main contributions of this paper can be summarized as follows:

(1) By means of topology optimization, the narrow-band restriction of the conventional coding metasurface is removed, and the main findings of this work are explained by the associated mechanisms of the internal resonances and the bianisotropy effect.

(2) A sector-scanning antenna with a rapid frequency variation of the wave source is designed, and the emission beams can fast scan a sector area periodically. This kind of frequency-angle scanning method can locate the azimuth of obstacles based on the echo frequency, and it can further locate the distance by the echo time. Of note, the design of the acoustic antenna is a fixed coding sequence, and its scanning and echolocation mode does not depend on the reconfiguration of the coding units.

(3) Through combining the two unit cells with out-of-phase responses, the BACMs can achieve a broadband diffusion scattering and its broadband validity also does not require a reconfiguration of the units.

As an outlook, if both phase and amplitude regulations are considered in the unit design [49,55,56], the performance of the metasurface regulation may achieve even higher efficiency. It should also be pointed out that the truly tunable and programmable acoustic metasurfaces in which the unit-cell patterns can be changed by a specific physical field (e.g., mechanical, electric, magnetic, thermal, and chemical, etc.) via a computer program without any human intervention [57,58], are very useful for controlling and reshaping a complex sound field automatically. Therefore, in our future work, we will combine the truly tunable and programmable approaches with the broadband coding metasurfaces to achieve broadband acoustic wave manipulation.

ACKNOWLEDGMENTS

This work is supported by the National Natural Science Foundation of China (Grants No. 11902171, No. 11802012, No. 12021002, No. 11991031, and No. 12172044), the Postdoctoral Science Foundation (2019M662297), the Sino-German Joint Research Project (Grant No. GZ 1355) and the German Research Foundation (DFG, Project No. ZH 15/27-1). H.W. Dong is also grateful for the support from the Research Fund Program for Young Scholars. The authors would like to sincerely thank one anonymous reviewer for highly valuable comments and constructive suggestions to improve the initial version of the paper.

APPENDIX: BIANISOTROPY VERIFICATION BY NUMERICAL SIMULATION

For the acoustic antenna in Fig. 5(f), we perform a bianisotropy verification based on the numerical simulation. In Fig. 12, we compare the results of Fig. 5(f) with that when the acoustic wave is incident from the opposite

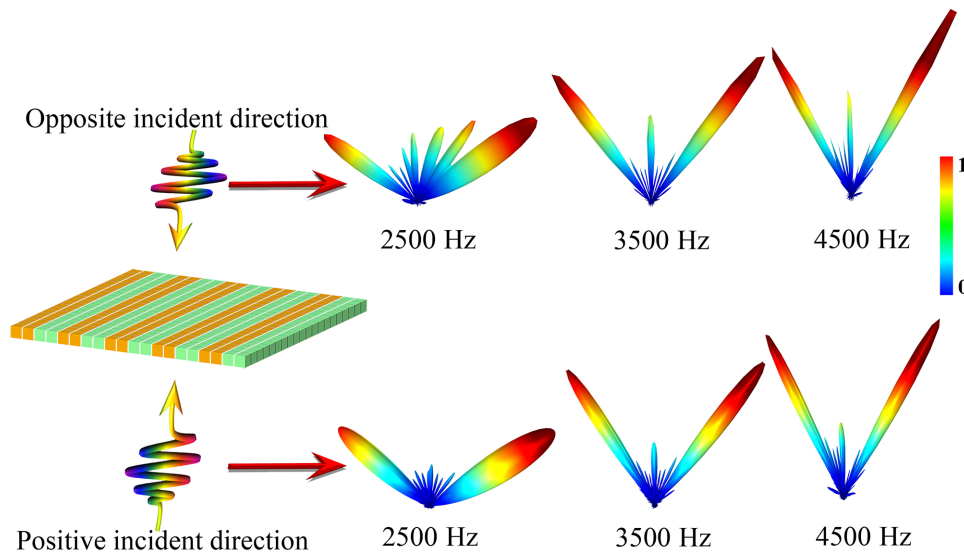


FIG. 12. The differences in the wave-scattering pattern caused by the bianisotropy when the acoustic wave is incident to the sector antenna from two opposite directions.

direction. The results clearly show that there is a significant difference between the results for the positive incident direction and the opposite incident direction, indicating that the bianisotropy effects exists.

-
- [1] S. A. Cummer, J. Christensen, and A. Alù, Controlling sound with acoustic metamaterials, *Nat. Rev. Mater.* **1**, 16001 (2016).
- [2] G. C. Ma and P. Sheng, Acoustic metamaterials: From local resonances to broad horizons, *Sci. Adv.* **2**, e1501595 (2016).
- [3] H. Ge, M. Yang, C. Ma, M. H. Lu, Y. F. Chen, N. Fang, and P. Sheng, Breaking the barriers: Advances in acoustic functional materials, *Nat. Sci. Rev.* **5**, 159 (2018).
- [4] B. Assouar, B. Liang, Y. Wu, Y. Li, J. C. Cheng, and Y. Jing, Acoustic metasurfaces, *Nat. Rev. Mater.* **3**, 460 (2018).
- [5] Z. H. Tian, C. Shen, J. F. Li, E. Reit, Y. Y. Gu, H. Fu, S. A. Cummer, and T. J. Huang, Programmable acoustic metasurfaces, *Adv. Funct. Mater.* **29**, 1808489 (2019).
- [6] H. T. Chen, A. J. Taylor, and N. Yu, A review of metasurfaces: Physics and applications, *Rep. Prog. Phys.* **79**, 076401 (2016).
- [7] S. D. Zhao, A. L. Chen, Y. S. Wang, and C. Zhang, Continuously Tunable Acoustic Metasurface for Transmitted Wavefront Modulation, *Phys. Rev. Appl.* **10**, 054066 (2018).
- [8] S. W. Fan, S. D. Zhao, A. L. Chen, Y. F. Wang, B. Assouar, and Y. S. Wang, Tunable Broadband Reflective Acoustic Metasurface, *Phys. Rev. Appl.* **11**, 044038 (2019).
- [9] A. L. Chen, Q. Y. Tang, H. Y. Wang, S. D. Zhao, and Y. S. Wang, Multifunction switching by a flat structurally tunable acoustic metasurface for transmitted waves, *Sci. China: Phys. Mech. Astron.* **63**, 244611 (2020).
- [10] Y. Li, C. Shen, Y. Xie, J. Li, W. Wang, S. A. Cummer, and Y. Jing, Tunable Asymmetric Transmission via Lossy Acoustic Metasurfaces, *Phys. Rev. Lett.* **119**, 035501 (2017).
- [11] Y. Q. Liu, Z. X. Liang, F. Liu, O. Diba, A. Lamb, and J. Li, Source Illusion Devices for Flexural Lamb Waves Using Elastic Metasurfaces, *Phys. Rev. Lett.* **119**, 034301 (2017).
- [12] Z. Liang and J. Li, Extreme Acoustic Metamaterial by Coiling up Space, *Phys. Rev. Lett.* **108**, 114301 (2012).
- [13] H. F. Zhu and F. Semperlotti, Anomalous Refraction of Acoustic Guided Waves in Solids with Geometrically Tapered Metasurfaces, *Phys. Rev. Lett.* **117**, 034302 (2016).
- [14] Y. Cheng, C. Zhou, B. G. Yuan, D. J. Wu, Q. Wei, and X. J. Liu, Ultra-sparse metasurface for high reflection of low-frequency sound based on artificial Mie resonances, *Nat. Mater.* **14**, 1013 (2015).
- [15] B. I. Popa, Y. Zhai, and H. S. Kwon, Broadband sound barriers with bianisotropic metasurfaces, *Nat. Commun.* **9**, 5299 (2018).
- [16] J. Li and J. B. Pendry, Hiding Under the Carpet: A New Strategy for Cloaking, *Phys. Rev. Lett.* **101**, 203901 (2008).
- [17] B. Orazbayev, N. M. Estakhri, M. Beruete, and A. Alù, Tera-hertz carpet cloak based on a ring resonator metasurface, *Phys. Rev. B* **91**, 195444 (2015).
- [18] M. Yang, S. Y. Chen, C. X. Fu, and P. Sheng, Optimal sound-absorbing structures, *Mater. Horiz.* **4**, 673 (2017).
- [19] Y. Zhu, X. Fan, B. Liang, J. C. Cheng, and Y. Jing, Ultrathin Acoustic Metasurface-based Schroeder Diffuser, *Phys. Rev. X* **7**, 021034 (2017).
- [20] X. Jiang, Y. Li, B. Liang, J. C. Cheng, and L. Zhang, Convert Acoustic Resonances to Orbital Angular Momentum, *Phys. Rev. Lett.* **117**, 034301 (2016).
- [21] Y. Fu, C. Shen, X. Zhu, J. Li, Y. Liu, S. A. Cummer, and Y. Xu, Sound vortex diffraction via topological charge in phase gradient metagratings, *Sci. Adv.* **6**, eaba9876 (2020).
- [22] J. Weng, Y. Ding, C. Hu, X. F. Zhu, B. Liang, J. Yang, and J. Cheng, Meta-neural-network for real-time and passive deep-learning-based object recognition, *Nat. Commun.* **11**, 6309 (2020).
- [23] K. Donda, Y. Zhu, A. Merkel, S. W. Fan, L. Cao, S. Wan, and B. Assouar, Ultrathin acoustic absorbing metasurface based on deep learning approach, *Smart Mater. Struct.* **30**, 085003 (2021).
- [24] C. D. Giovampaola and N. Engheta, Digital metamaterials, *Nat. Mater.* **13**, 1115 (2014).
- [25] T. J. Cui, M. Q. Qi, X. Wan, J. Zhao, and Q. Cheng, Coding metamaterials, digital metamaterials and programmable metamaterials, *Light Sci. Appl.* **3**, e218 (2014).
- [26] L. Zhang, X. Q. Chen, S. Liu, Q. Zhang, J. Zhao, J. Y. Dai, G. D. Bai, X. Wan, Q. Cheng, G. Castaldi, V. Galdi, and T. J. Cui, Space-time-coding digital metasurfaces, *Nat. Commun.* **9**, 4334 (2018).
- [27] B. Y. Xie, K. Tang, H. Cheng, Z. Y. Liu, S. Q. Chen, and J. G. Tian, Coding acoustic metasurfaces, *Adv. Mater.* **29**, 1603507 (2017).
- [28] Q. Ma, C. B. Shi, G. D. Bai, T. Y. Chen, A. Noor, and T. J. Cui, Beam-editing coding metasurfaces based on polarization bit and orbital-angular-momentum-mode bit, *Adv. Opt. Mater.* **5**, 1700548 (2017).
- [29] Y. Zhang, H. Cheng, J. G. Tian, and S. Q. Chen, Frequency-selected Bifunctional Coding Acoustic Metasurfaces, *Phys. Rev. Appl.* **14**, 064057 (2020).
- [30] X. D. Fan, Y. F. Zhu, B. Liang, J. Yang, and J. C. Cheng, Broadband convergence of acoustic energy with binary reflected phase on planar surface, *Appl. Phys. Lett.* **109**, 243501 (2016).
- [31] H. Tang, Z. Chen, N. Tang, S. Li, Y. Shen, Y. Peng, X. Zhu, and J. Zang, Hollow-out patterning ultrathin acoustic metasurfaces for multifunctionalities using soft fiber/rigid bead networks, *Adv. Funct. Mater.* **28**, 1801127 (2018).
- [32] L. H. Gao, Q. Cheng, J. Yang, S. J. Ma, J. Zhao, S. Liu, H. B. Chen, Q. He, W. X. Jiang, H. F. Ma, Q. Y. Wen, L. J. Liang, B. B. Jin, W. W. Liu, L. Zhou, J. Q. Yao, P. H. Wu, and T. J. Cui, Broadband diffusion of terahertz waves by multi-bit coding metasurfaces, *Light Sci. Appl.* **4**, e324 (2015).
- [33] M. Moccia, S. Liu, R. Y. Wu, G. Castaldi, A. Andreone, T. J. Cui, and V. Galdi, Coding metasurfaces for diffuse scattering: Scaling laws, bounds, and suboptimal design, *Adv. Opt. Mater.* **5**, 1700455 (2017).
- [34] X. M. Yang, X. Y. Zhou, Q. Cheng, H. F. Ma, and T. J. Cui, Diffuse reflections by randomly gradient index metamaterials, *Opt. Lett.* **35**, 808 (2010).

- [35] X. D. Fan, Y. F. Zhu, B. Liang, J. Yang, J. Yang, and J. C. Cheng, Ultra-broadband and planar sound diffuser with high uniformity of reflected intensity, *Appl. Phys. Lett.* **111**, 103502 (2017).
- [36] S. Wang, P. C. Wu, V. C. Su, Y. C. Lai, C. H. Chu, J. W. Chen, S. H. Lu, J. Chen, B. Xu, C. H. Kuan, T. Li, S. Zhu, and D. P. Tsai, Broadband achromatic optical metasurface devices, *Nat. Commun.* **8**, 187 (2017).
- [37] W. T. Chen, A. Y. Zhu, V. Sanjeev, M. Khorasaninejad, Z. Shi, E. Lee, and F. Capasso, A broadband achromatic metalens for focusing and imaging in the visible, *Nat. Nanotechnol.* **13**, 220 (2018).
- [38] S. Wang, P. C. Wu, V. C. Su, Y. C. Lai, M. K. Chen, H. Y. Kuo, B. H. Chen, Y. H. Chen, T. T. Huang, J. H. Wang, R. M. Li, C. H. Kuan, T. Li, Z. Wang, S. Zhu, and D. P. Tsai, A broadband achromatic metalens in the visible, *Nat. Nanotechnol.* **13**, 227 (2018).
- [39] S. Shrestha, A. C. Overvig, M. Lu, A. Stein, and N. Yu, Broadband achromatic dielectric metalenses, *Light-Sci. Appl.* **7**, 85 (2018).
- [40] H. W. Dong, S. D. Zhao, Y. S. Wang, and C. Zhang, Topology optimization of anisotropic broadband double-negative elastic metamaterials, *J. Mech. Phys. Solids* **105**, 54 (2017).
- [41] H. W. Dong, S. D. Zhao, P. Wei, L. Cheng, Y. S. Wang, and C. Zhang, Systematic design and realization of double-negative acoustic metamaterials by topology optimization, *Acta Mater.* **172**, 102 (2019).
- [42] H. T. Zhou, W. X. Fu, Y. F. Wang, Y. S. Wang, V. Laude, and C. Zhang, Ultra-broadband passive acoustic metasurface for wide-angle carpet cloaking, *Mater. Des.* **199**, 109414 (2021).
- [43] H. W. Dong, S. D. Zhao, C. Shen, W. B. Qiu, Y. S. Wang, L. Cheng, C. Zhang, H. R. Zheng, and S. A. Cummer, Achromatic metasurfaces with inversely customized dispersion for ultra-broadband acoustic beam engineering, *Natl. Sci. Rev.* (2022).
- [44] N. J. Gerard, H. Cui, C. Shen, Y. Xie, S. V. Cummer, X. Zheng, and Y. Jing, Fabrication and experimental demonstration of a hybrid resonant acoustic gradient index metasurface at 40 kHz, *Appl. Phys. Lett.* **114**, 231902 (2019).
- [45] Y. Jin, R. Kumar, O. Poncelet, O. Mondain-Monval, and T. Brunet, Flat acoustics with soft gradient-index metasurfaces, *Nat. Commun.* **10**, 143 (2019).
- [46] E. Bok, J. J. Park, H. Choi, C. K. Han, O. B. Wright, and S. H. Lee, Metasurface for Water-to-Air Sound Transmission, *Phys. Rev. Lett.* **120**, 044302 (2018).
- [47] Z. Huang, S. D. Zhao, Y. Zhang, Z. Cai, Z. Li, J. Xiao, M. Su, Q. Guo, C. Zhang, Y. Pan, X. Cai, Y. Song, and J. Yang, Tunable fluid-type metasurface for wide-angle and multi-frequency water-air acoustic transmission, *Research* **2021**, 9757943 (2021).
- [48] B. H. Song and J. S. Bolton, A transfer-matrix approach for estimating the characteristic impedance and wave numbers of limp and rigid porous materials, *J. Acoust. Soc. Am.* **107**, 1131 (2000).
- [49] J. Li, C. Shen, A. Díaz-Rubio, S. A. Tretyakov, and S. A. Cummer, Systematic design and experimental demonstration of bianisotropic metasurfaces for scattering-free manipulation of acoustic wavefronts, *Nat. Commun.* **9**, 1342 (2018).
- [50] S. Liu, T. J. Liu, L. Zhang, Q. Xu, Q. Wang, X. Wan, J. Q. Gu, W. X. Tang, M. Q. Qi, J. G. Han, W. L. Zhang, X. Y. Zhou, and Q. Cheng, Convolution operations on coding metasurface to reach flexible and continuous controls of terahertz beams, *Adv. Sci.* **3**, 1600156 (2016).
- [51] Y. Chen, X. N. Liu, and G. K. Hu, Latticed pentamode acoustic cloak, *Sci. Rep.* **5**, 15745 (2015).
- [52] Y. Li and B. Assouar, Acoustic metasurface-based perfect absorber with deep subwavelength thickness, *Appl. Phys. Lett.* **108**, 063502 (2016).
- [53] D. S. Dong, J. Yang, Q. Cheng, J. Zhao, L. H. Gao, S. J. Ma, S. Liu, H. B. Chen, Q. He, W. W. Liu, Z. Fang, L. Zhou, and T. J. Cui, Terahertz broadband low-reflection metasurface by controlling phase distributions, *Adv. Opt. Mater.* **3**, 1405 (2015).
- [54] Y. Zhao, X. Cao, J. Gao, Y. Sun, H. Yang, X. Liu, Y. Zhou, T. Han, and W. Chen, Broadband diffusion metasurface based on a single anisotropic element and optimized by the simulated annealing algorithm, *Sci. Rep.* **6**, 23896 (2016).
- [55] L. Quan and A. Alù, Passive Acoustic Metasurface with Unitary Reflection Based on Nonlocality, *Phys. Rev. Appl.* **11**, 054077 (2019).
- [56] Y. Zhu, N. J. Gerard, X. Xia, G. C. Stevenson, L. Cao, S. Fan, C. M. Spadaccini, Y. Jing, and B. Assouar, Systematic design and experimental demonstration of transmission-type multiplexed acoustic metaholograms, *Adv. Funct. Mater.* **31**, 2101947 (2021).
- [57] W. K. Cao, C. Zhang, L. T. Wu, K. Q. Guo, J. C. Ke, T. J. Cui, and Q. Cheng, Tunable Acoustic Metasurface for Three-Dimensional Wave Manipulations, *Phys. Rev. Appl.* **15**, 024026 (2021).
- [58] G. Ma, X. Fan, P. Sheng, and M. Fink, Shaping reverberating sound fields with an actively tunable metasurface, *Proc. Natl. Acad. Sci.* **115**, 6638 (2018).